nature communications

Article

https://doi.org/10.1038/s41467-024-55753-2

Floatable artificial leaf to couple oxygen-tolerant CO_2 conversion with water purification

Received: 18 September 2024

Accepted: 24 December 2024

Published online: 02 January 2025

Check for updates

Zhiyong Zhang[1,2], Yang Wang[2,3], Yangen Xie[1,2], Toru Tsukamoto[1,2], Qi Zhao[1,2], Qing Huang[1,2], Xingmiao Huang[1,2], Boyang Zhang[1,2], Wenjing Song[1,2], Chuncheng Chen[1,2], Hua Sheng[1,2] ✉ & Jincai Zhao[1,2]

To enable open environment application of artificial photosynthesis, the direct utilization of environmental CO_2 via an oxygen-tolerant reductive procedure is necessary. Herein, we introduce an in situ growth strategy for fabricating two-dimensional heterojunctions between indium porphyrin metal-organic framework (In-MOF) and single-layer graphene oxide (GO). Upon illumination, the In-MOF/GO heterostructure facilitates a tandem CO_2 capture and photocatalytic reduction on its hydroxylated In-node, prioritizing the reduction of dilute CO_2 even in the presence of air-level O_2. The In-MOF/GO heterostructure photocatalyst is integrated with a porous polytetrafluoroethylene (PTFE) membrane to construct a floatable artificial leaf. Through a triphase photocatalytic reaction, the floatable artificial leaf can remove aqueous contaminants from real water while efficiently reducing CO_2 at low concentrations (10%, approximately the CO_2 concentration in combustion flue gases) upon air-level O_2. This study provides a scalable approach for the construction of photocatalytic devices for CO_2 conversion in open environments.

As a method for direct solar energy utilization, light-driven systems have garnered significant interest in sustainable energy conversion and environmental treatment[1–5]. Compared to thermal and electrocatalytic systems, light-driven systems are more advantageous in terms of energy supply needs. Powered directly by sunlight, light-driven systems minimize the need for complex external energy supplies, rendering the construction of photocatalytic devices easier and less constrained by location and space requirements[6–10]. Recently, Reisner et al. demonstrated a floatable artificial leaf integrating perovskite-$BiVO_4$ catalysts that facilitates energy conversion processes[7], such as water splitting, to be conducted in open water, thereby avoiding competition with land use. This innovative approach leveraged the flexibility of light-driven systems and offers new possibilities for practical applications in open environments. Additionally, floatable photocatalytic systems, which operate at the gas-water interface, have the potential to combine energy conversion, such as reducing water or CO_2 into fuels, with water purification via oxidative removal of aqueous contaminants, demonstrating a promising direction for photocatalysis-based applications (Fig. 1). However, for these open environment applications to be feasible, the reductive energy conversion reactions must be tolerant to oxygen, as atmospheric oxygen competes for electrons[11–16].

In artificial photosynthesis, which photo-catalytically converts CO_2 into fuels and industrial feedstocks to recycle excess CO_2 emissions, the use of concentrated and oxygen-free CO_2 gas is typically necessary to eliminate the competition from the thermodynamically more favorable O_2 reduction reaction ($E_{CO2/CO} = -0.53$ V vs. $E_{O2/H2O} = 1.23$ V)[17–22]. Despite the significant challenges, developing oxygen-tolerant photocatalytic CO_2 conversion is highly beneficial for direct utilization of environmental CO_2, such as air (containing 0.04% CO_2

[1]Key Laboratory of Photochemistry, Institute of Chemistry Chinese Academy of Sciences, Beijing National Laboratory for Molecular Sciences, Beijing, PR China. [2]University of Chinese Academy of Sciences, Beijing, PR China. [3]CAS Key Laboratory of Green Process and Engineering, Institute of Process Engineering, Chinese Academy of Sciences, Beijing, PR China. ✉e-mail: hsheng@iccas.ac.cn

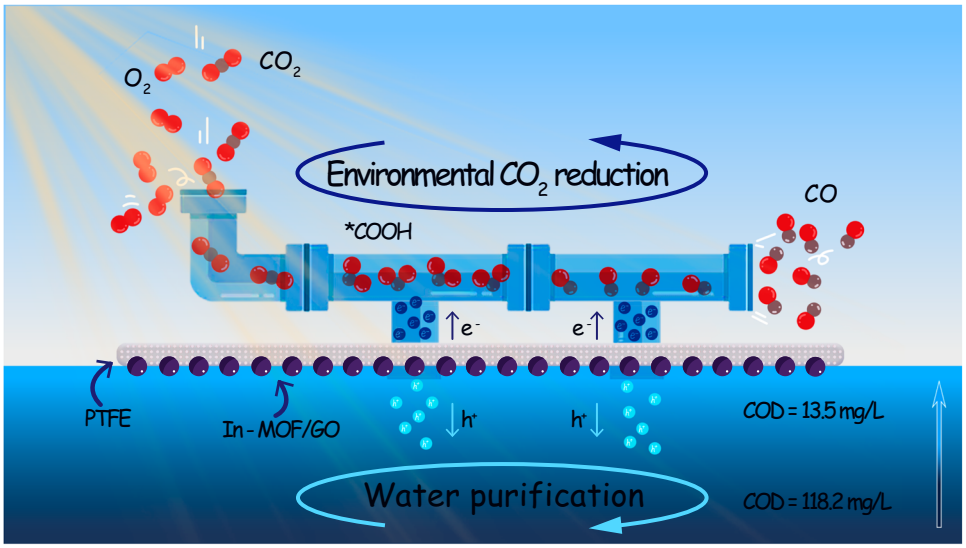

Fig. 1 | Schematic illustration of the catalyst application. Schematic illustration depicting the design of a floatable artificial leaf to function as an integrated system for environmental CO_2 reduction and water purification.

and 20.9% O_2) or combustion flues (typically containing 12–14% CO_2 and 3–5% O_2)[23–25], thereby circumventing the energy-intensive and time-consuming procedures required for CO_2 capture and enrichment. Learning from natural photosynthesis, where the enzyme RuBisCO in the Calvin cycle plays a crucial role in selective capturing and retaining CO_2 for further reduction[26], a promising approach for developing oxygen-tolerant photocatalytic CO_2 reduction (CO_2RR) involves a similar mechanism. A suitable photocatalyst should facilitate a tandem process that preferentially captures CO_2 and then reduces it at specific surface sites.

In this study, we fabricated a two-dimensional (2D) heterostructure between an indium-based porphyrin metal–organic framework (In-MOF) and graphene oxide (GO) via an in situ approach. In the In-MOF moiety, the surface-hydroxyl-enriched In-nodes prioritize capturing CO_2 over O_2. The internal electron transfer within the heterostructure further facilitates the activation of the captured CO_2 on the same surface sites for further conversion. The fabricated 2D heterostructure was integrated with a hydrophobic and floatable polytetrafluoroethylene (PTFE) membrane to develop artificial leaves. The developed floatable device enabled the coupling of environmental CO_2 reduction and water purification processes. Notably, even at low CO_2 concentrations (~10%, which is approximately the CO_2 concentration in combustion flue gases) under air-level O_2, the floatable device reduced CO_2 to CO with 100% selectivity at a rate of 762.5 $\mu mol \cdot g^{-1} \cdot h^{-1}$. Simultaneously, this process reduced the COD of natural water bodies from 118.2 mg/L to 13.5 mg/L, meeting the class I water standard of China. This study provides a scalable approach for fabricating photocatalytic devices for CO_2 conversion in open environments.

Results

Characterization of photocatalysts

The in situ growth of 2D In-MOF on single-layered GO was triggered by separately injecting aqueous solutions of $In(NO_3)_3$ and tetrakis(4-carboxylpheny) porphyrin (TCPP), the precursors of In-MOF, into a GO suspension dispersed in a DMF/EtOH mixture (V/V = 3/1) (Fig. 2a). The injection rates of both precursor solutions were precisely controlled at a rate of 0.25 $mL \cdot h^{-1}$ using an injection pump and injection rates that are too fast or too slow can affect the formation of In-MOF/GO (Supplementary Fig. 1). The growth procedure was performed for 6 h; samples were collected hourly for monitoring using transmission electron microscopy (TEM) and X-ray diffraction (XRD). The samples were named In-MOF/GO-xh, where x denotes the hour after which the sample was taken. The pristine GO sheet (In-MOF/GO-0h) has a clean surface with a typical layered structure (Fig. 2b), characterized by a single XRD peak at 11.4° corresponding to the (100) plane[27] (Fig. 2c). The absence of additional peaks in the XRD patterns (Fig. 2c; In-MOF/GO-0h and In-MOF/GO-2h) indicates that during the first 2 h of in situ growth only small In-MOF nuclei, which have not crystallized, are present on the GO sheet (Fig. 2b). Prolonged growth for more than 3 h results in the formation of a sheet-like 2D In-MOF with its characteristic XRD peak at 7.5° assigned to the (021) plane of In-MOF[28,29]. After 4 h of growth, cubic nanosheets of In-MOF are clearly observed to be well-dispersed on the GO surface in a face-to-face arrangement, forming a well-defined 2D/2D heterojunction. In Fig. 2c, the well-resolved (021) peak in the XRD pattern of In-MOF/GO-4h demonstrates full crystallization of the 2D In-MOF. After 6 h of elapsed growth time, the GO surface becomes fully occupied by In-MOF nanosheets, aggregated in random orientations (Fig. 2b; In-MOF/GO-6h). Notably, the synthetic approach for In-MOF nanosheets presented in this study is a modified version of a previously reported procedure[28]. The XRD patterns (Fig. 2c) of the as-synthesized In-MOF nanosheets match well with those of the previously reported In-MOF (Supplementary Fig. 2b). As shown in Supplementary Fig. 2c and d, the previously reported In-MOF contains In-nodes coordinated with four oxygen atoms from the basal plane ligands and two oxygen atoms from the axial OH groups, forming $InO_4(OH)_2$ chains[28].

The In-MOF/GO-4h sample, featuring well-dispersed In-MOF nanosheets without aggregation, was further characterized. High-resolution TEM (HR-TEM) analysis reveals a lattice fringe of 1.153 nm (Fig. 2d), corresponding to the (021) plane of In-MOF[28] (Supplementary Fig. 3). High-angle annular dark-field (HAADF) mapping showed that the 2D In-MOF formed a face-to-face dominant architecture on the GO sheet (Fig. 2e). Atomic force microscopy (AFM) was used to estimate the thickness of the 2D In-MOF. The thickness of the in situ grown In-MOF nanosheets is determined to be approximately 0.8 nm (Supplementary Fig. 4).

Photocatalytic activity test

The artificial leaf was constructed by integrating 2 mg of the synthesized In-MOF/GO composite into the hydrophobic pore structure of a PTFE membrane through vacuum filtration. This artificial leaf could float on water and initiate a triphase photocatalytic process (Fig. 3a). After orienting the In-MOF/GO catalyst-embedded side of the artificial leaf downward and the other side with an open pore structure upward,

https://doi.org/10.1038/s41467-024-55753-2

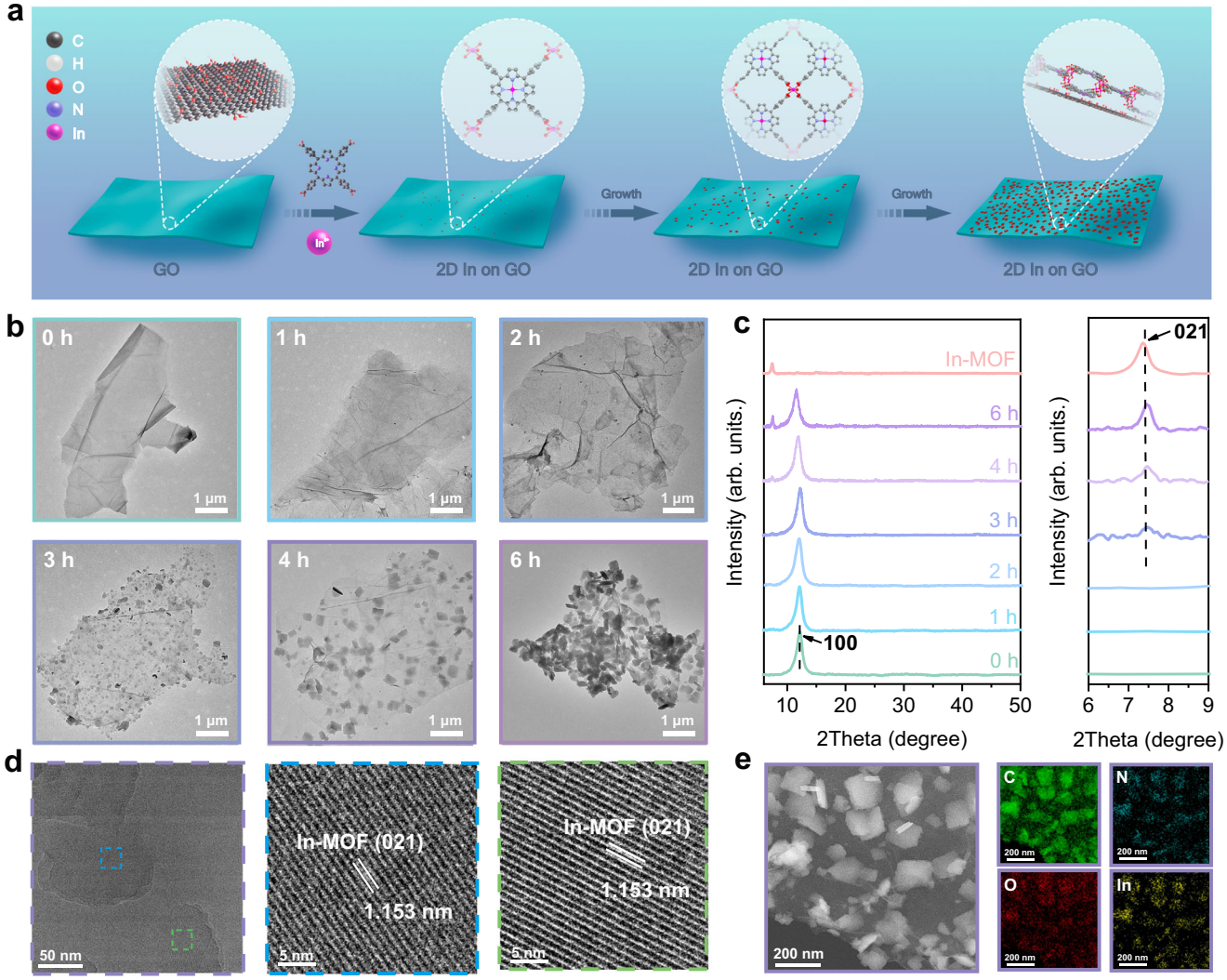

Fig. 2 | Characterization of 2D In-MOF/GO. a Schematic showing the synthesis process of In-MOF/GO. **b** TEM images and **c** XRD at indicated elapsed growth time, the red spectrum in Fig.1c represents the synthesized In-MOF nanosheets. **d** HR-TEM images and **e** HAADF mapping of In-MOF/GO-4h, where 4 h represents the elapsed growth time. Source data for Fig. 2c is provided as a Source Data file.

the hydrophobic pore structure of the integrated system can function as a gas-diffusion layer to facilitate the transportation of gaseous reagents to the embedded catalysts. Integration of MOF into a floatable device rather than simply dispersing it in an aqueous phase enhances the effect of the MOF pore structure in enriching gaseous reagents. The limited solubility of CO_2 in water renders floatable photocatalytic devices beneficial for reactions involving sources with low CO_2 concentrations. The triphase photocatalysis was first conducted in deionized water with 10% CO_2 (mimicking typical CO_2 levels in combustion flue gases), 0–20% O_2, and 90–70% Ar in the gas phase. Even in the presence of air-level O_2 (20%), the artificial leaf demonstrated a high CO generation rate of 762.5 $\mu mol \cdot g^{-1} \cdot h^{-1}$ with 100% selectivity, without notable H_2 generation[30]. Furthermore, the catalyst loading has minimal impact on catalytic activity. Even with an increase in In-MOF/GO loading from 2 to 20 mg, the mass-dependent CO generation rate decreased by only approximately 9% (Supplementary Fig. 5). The performance demonstrated by the constructed artificial leaf under aerobic conditions surpasses the performances of most reported MOF-based and inorganic catalysts under anaerobic conditions (Supplementary Table 1).

For photocatalytic CO_2 reduction, the use of artificial leaves loaded with In-MOF/GO-4h exhibits 20.3 and 32.9 times higher CO generation rates than those of In-MOF or GO, respectively (Fig. 3b). It is worth noting the aim of in situ growth approach is to facilitate a "good-contact" between In-MOF and GO, which is crucial in enhancing photocatalytic performances of heterostructure. Instead, when using an ex situ approach to fabricate In-MOF/GO heterostructure from the mixed suspension of GO and pre-synthesized In-MOF (referred to as In-MOF/GO-ex-situ; Supplementary Fig. 6), its activity was very limited, with no notable improvement compared to individual In-MOF or GO (Fig. 3b). Notably, when MOF/GO-4h powders were directly dispersed in water and tested for photocatalytic activity without being integrated into a floatable device, a significant decrease in the CO generation rate (87.5 $\mu mol \cdot g^{-1} \cdot h^{-1}$) was observed (Supplementary Fig. 7), highlighting the clear advantage of employing a floatable system. Moreover, the duration of in situ growth remarkably affects the reaction performance[31], as evident from Supplementary Fig. 8. Among the heterostructures with different in situ growth durations, In-MOF/GO-4h exhibits the highest photocatalytic performance, highlighting the importance of kinetically controlled growth of In-MOF on GO.

To confirm the source of CO generation, control experiments were conducted without light, photocatalyst, or CO_2; none of these experiments generated CO (Supplementary Fig. 9). In addition, using $^{13}CO_2$ instead of $^{12}CO_2$, the peak at m/z = 29 (^{13}CO) in the MS spectrum confirms that the source of C in CO originates from CO_2 (Fig. 3c). Further, the stability of In-MOF/GO-4h was tested; even after five cycles

https://doi.org/10.1038/s41467-024-55753-2

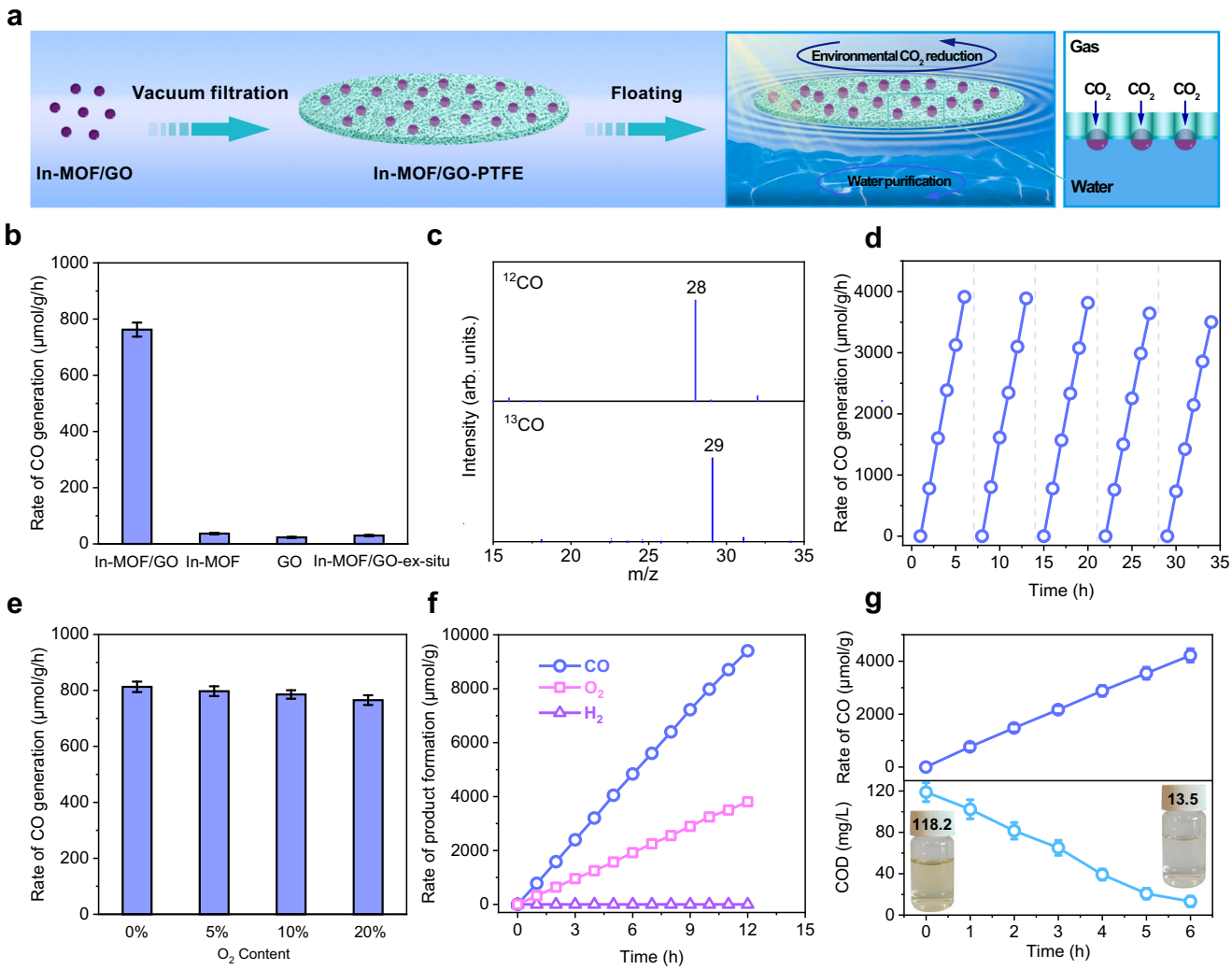

Fig. 3 | Photocatalytic activity of the floatable artificial leaf loaded with In-MOF/GO. a Schematic showing the photocatalytic reaction on a floatable artificial leaf loaded with In-MOF/GO. **b** Comparison of the CO generation rates from aerobic CO_2 reduction using In-MOF/GO-4h synthesized via in situ growth, In-MOF, GO, and In-MOF/GO synthesized via ex situ assembly. **c** GC-MS spectra of CO produced on In-MOF/GO-4h using ordinary $^{12}CO_2$ and $^{13}CO_2$. **d** Cycling test results of aerobic CO_2 photoreduction on In-MOF/GO-4h. **e** Dependence of CO generation rate on O_2 levels. **f** Product generation rates of oxidative half-reaction products in the In-MOF/GO-4h loaded artificial leaves under oxygen-free conditions. **g** CO generation rate as a function of time obtained from coupling of aerobic CO_2 reduction with water purification; the lower section displays the variation of COD in lake water during photoreactions, the inset shows photographic images of the lake water before and after purification. The error bar represents the standard deviation of the measurements. Reaction conditions: For **b**, **c**, **d**, and **g**, the gas atmosphere was 10% CO_2, 20% O_2 and 70% Ar; for (**e**), O_2 level ranged from 0% to 20%, balanced with Ar; for (**f**), the atmosphere was O_2-free (10% CO_2 and 90% Ar). For **b**–**f**, deionized water was used, whereas lake water collected from Beijing Olympic Park was employed for (**g**). Source data for Fig. 3b–g are provided as a Source Data file.

of aerobic CO_2 photoreduction, the catalyst still maintains 95% efficiency (Fig. 3d). Characterization of In-MOF/GO-4h after five cycles shows almost undetectable variations in the morphological, crystallographic, or chemical structure and no detachment or aggregation of the In-MOF nanosheets (Supplementary Figs. 10–12). Next, the intrinsic relationship between O_2 concentration and CO_2RR rate was explored. The results reveal that, compared to an oxygen-free environment, the decline in the efficiency of aerobic CO_2RR efficiency is very limited. Notably, even when the oxygen concentration reaches 20%, In-MOF/GO still exhibits remarkable efficiency and the CO generation rate decreased by only 5% compared to that in an oxygen-free environment. This finding demonstrates the excellent tolerance and efficiency of In-MOF/GO in performing the CO_2RR under aerobic conditions, maintaining a high catalytic activity despite the interference from elevated levels of oxygen.

Furthermore, to monitor the products of oxidative half-reactions in the In-MOF/GO−4h loaded artificial leaves, we measured the generated O_2 during photoreaction in an oxygen-free atmosphere containing 10% CO_2 and 90% Ar. Along with the generation of CO from CO_2 reduction, O_2 derived from water oxidation was also observed. The generation of products follows a linear growth that persists for 12 h (Fig. 3f). The observed ratio between the generation rates of CO (762.5 $\mu mol \cdot g^{-1} \cdot h^{-1}$) and O_2 (321.8 $\mu mol \cdot g^{-1} \cdot h^{-1}$) is higher than the corresponding stoichiometric ratio of 2, suggesting the existence of another product from the oxidative half-reactions. Therefore, we next measured the possible liquid products of the photocatalytic reactions. No liquid products, such as formic acid, are generated by the CO_2RR half-reaction; however, H_2O_2 is generated at a generation rate of 232.5 $\mu mol \cdot g^{-1} \cdot h^{-1}$. Notably, the amount of generated H_2O_2 is not affected by the O_2 content in the atmosphere. Only a slight reduction of 5% in H_2O_2 generation rate is observed when the O_2 ratio in the atmosphere increases from 0% to 20% (Supplementary Fig. 13). Therefore, H_2O_2 is mostly likely generated by water oxidation. This further explains the discrepancy between the observed ratios of generation rates and stoichiometric values between CO and O_2 and when comparing to the literature

reports, this floating system exhibits superior activity in the H_2O_2 generation originated from water oxidation[10,32,33].

Owing to the generation of H_2O_2, a widely used reagent in aqueous pollutant degradation and sterilization, on the floatable artificial leaves, we considered coupling aerobic CO_2 reduction with water purification for real environmental applications. We collected lake water from Beijing Olympic Park and used it with our floatable device in an atmosphere containing 10% CO_2, 20% O_2 and 70% Ar. Supplementary Fig. 14 shows the photocatalytic reactor setup used for purification of water. In both deionized water and lake water, the floatable device exhibits identical performance in the aerobic photocatalytic CO_2 reduction to CO, indicating that the presence of organic or inorganic substances in lake water does not interfere with CO_2 reduction activity (Fig. 3g, upper part). Next, we monitored the variations in Chemical Oxygen Demand (COD) of lake water during the photocatalytic reaction. The COD values (Fig. 3g, lower part) decrease linearly with illumination time, suggesting the decomposition of organic contaminants by the in situ generated H_2O_2 or photogenerated holes. The in situ EPR analysis also confirmed the presence of hydroxyl radicals, which may also contribute to the removal of aqueous contaminants (Supplementary Fig. 15). After 6 h, the COD of the lake water falls below 15 mg/L, meeting class I water standard of China (Supplementary Fig. 16). Hence, the design of the floatable artificial leaves provides a facile reaction system suitable for use in open water environments.

Investigation of preferential CO_2 adsorption

Next, we investigated the origin of the aerobic photocatalytic CO_2 reduction by In-MOF/GO. First, we investigated electron transfer between the two moieties of In-MOF/GO. The bandgaps of In-MOF and GO were determined using Tauc plots derived from UV–vis spectroscopy, while the conduction band potentials were established through Mott-Schottky analysis, allowing for the construction of the band structure diagram. In-MOF exhibits a less negative conduction band level (−0.9 V vs. NHE) compared to GO (−1.0 V), but a more positive valence band level (2.0 V vs. NHE) than GO (1.8 V). As a result, they are likely to form a type-II heterojunction, with the electron transfer occurring from GO to In-MOF and hole transfer from In-MOF to GO (Supplementary Fig. 17). The formation of the heterojunction was further confirmed by photocurrent and electrochemical impedance spectroscopy (EIS) measurements, which indicate that the hybrid In-MOF/GO exhibits significantly enhanced electron-hole separation capabilities compared to individual In-MOF or GO (Supplementary Fig. 18).

Further, density functional theory-based calculations performed using the In-MOF/GO heterostructure model show that electron densities on the GO and In-MOF moieties decrease and increase, respectively, indicating electron transfer from GO to In-MOF during the formation of the heterostructure (Supplementary Fig. 19). This theoretical result corroborates well with the X-ray photo-electron spectra (XPS) results. In the In-MOF/GO composite material, a shift in the C 1*s* peak of GO toward higher binding energies occurs simultaneously with the counter-directional shift of the In 3*d* peak of In-MOF. This phenomenon indicates electron transfer from GO to In-MOF within the heterostructure (Supplementary Fig. 20).

In the theoretical model of In-MOF/GO, after placing a CO_2 molecule and subsequent structural optimization, the analysis of electron density overlap between the CO_2 molecule and axial hydroxyl on the In node in In-MOF reveals the capability of the surface hydroxyl to capture molecular CO_2. After the attachment of CO_2 to the hydroxyl group of the In-node in the In-MOF/GO heterostructure, CO_2 receives partial electrons from both GO (0.40 e^-) and In-MOF (0.05 e^-) moieties (Fig. 4a). In this case, the total electrons transferred (0.45 e^-) to CO_2 are significantly higher than those when CO_2 is attached to a self-supported In-MOF (0.13 e^-), as depicted in Fig. 4b. Thus, the adsorption energy of CO_2 on an In-MOF/GO heterostructure sharply decreases to −0.57 eV, indicating a more stable CO_2 capture compared to the adsorption energy of CO_2 on a self-supported In-MOF (−0.11 eV), as shown in Fig. 4c. Investigations on the interactions between O_2 and In-MOF/GO reveal that the surface sites of In-MOF/GO, including the surface hydroxyl groups, are almost inert to O_2 adsorption (endothermic by ~0.09 eV). In conclusion, the heterostructure of In-MOF/GO significantly enhances the capture of CO_2 over O_2, which is crucial for aerobic photocatalytic CO_2 reduction.

The interaction between CO_2 and the surface hydroxyl groups of the In-node of In-MOF was further analyzed using in situ Fourier Transform infrared spectroscopy (FT-IR) (Supplementary Fig. 21). The FT-IR results show that when CO_2 is introduced, the intensity of the IR peak located at 3612 cm^{-1}, attributed to the hydroxyl on the In node[34], gradually decreases. Simultaneously, a new band at 2347 cm^{-1} emerges and gradually becomes prominent. This band, which is different from the doublet gaseous CO_2 band, has a singlet feature and frequency close to those of dissolved CO_2 in an aqueous solution (solvated CO_2 by forming hydrogen bonds with the water solvent)[35]. Therefore, this band can be assigned to CO_2 interacting with surface hydroxyl groups via hydrogen bonding. The FT-IR results further confirm the interaction between the hydroxyl groups on the In-node and CO_2, facilitating CO_2 capture on In-MOF/GO. In conclusion, the surface hydroxyl groups on In-MOF/GO facilitate the selective capture and enrichment of CO_2.

The adsorption−desorption curves of CO_2 and O_2 on In-MOF/GO at 1 atm show adsorption capacities of 18.21 cm^3/g and 1.62 cm^3/g for CO_2 and O_2, respectively (Fig. 4d). Considering the composition of the gaseous atmosphere used in our aerobic photocatalytic CO_2 reduction, we compared the results obtained at 0.1 and 0.2 atm for CO_2 and O_2, respectively. Analysis of the initial slopes of the adsorption isotherms at these specified pressures reveals an approximate selectivity ratio of 30 for CO_2 versus O_2 adsorption on In-MOF/GO. This finding strongly supports the superior adsorption capacity of In-MOF/GO for CO_2 compared to O_2. Furthermore, we conducted temperature-programmed desorption (TPD) experiments to verify the preferential adsorption capability of CO_2 (Supplementary Fig. 22). The results showed that CO_2 exhibited a larger desorption peak area and a higher desorption temperature compared to O_2, indicating that In-MOF/GO possesses strong selectivity and stability for CO_2 adsorption, allowing it to preferentially adsorb CO_2 even in the presence of competing gases such as O_2.

Photocatalytic reaction mechanism

To elucidate the mechanism of CO_2 reduction on In-MOF/GO, we collected in situ FT-IR spectra during the photocatalytic reactions. The reaction was first conducted under oxygen-free conditions in a D_2O-saturated gas atmosphere containing 10% CO_2 and 90% Ar. The strategic use of D_2O instead of H_2O precludes the masking effect of the intense H_2O bending vibration band (~1630 cm^{-1}), enabling a clear identification of the characteristic bands from the MOF structure, such as the carboxylate/carboxylic acid moiety. Additionally, a parallel ^{13}C-isotope labeling experiment was conducted using $^{13}CO_2$ instead of $^{12}CO_2$ to identify the origin of the IR band, from CO_2-related intermediates or structural variations in the MOF structure. Upon illumination, a gradual depletion of intensity at 1206 cm^{-1}, attributed to the bending vibration of D_2O, indicates the oxidative consumption of water (Fig. 5b). Based on the presence of ^{13}C-isotope shift, the newly emerged bands can be classified into two groups. The bands at 1631 and 1376 cm^{-1} exhibit their ^{13}C-counterparts at 1599 and 1344 cm^{-1}, respectively (Fig. 5c). These bands can be assigned to *COOH[36–38], a vital intermediate in the reduction of CO_2 to CO. Notably, the band at 1631 cm^{-1} observed under $^{12}CO_2$ exhibits a right shoulder at ~1658 cm^{-1}. Under $^{13}CO_2$, the band at 1631 cm^{-1} shifts to 1599 cm^{-1}, appearing as a negative peak. Based on the standard IR spectrum of In-MOF, the band

https://doi.org/10.1038/s41467-024-55753-2

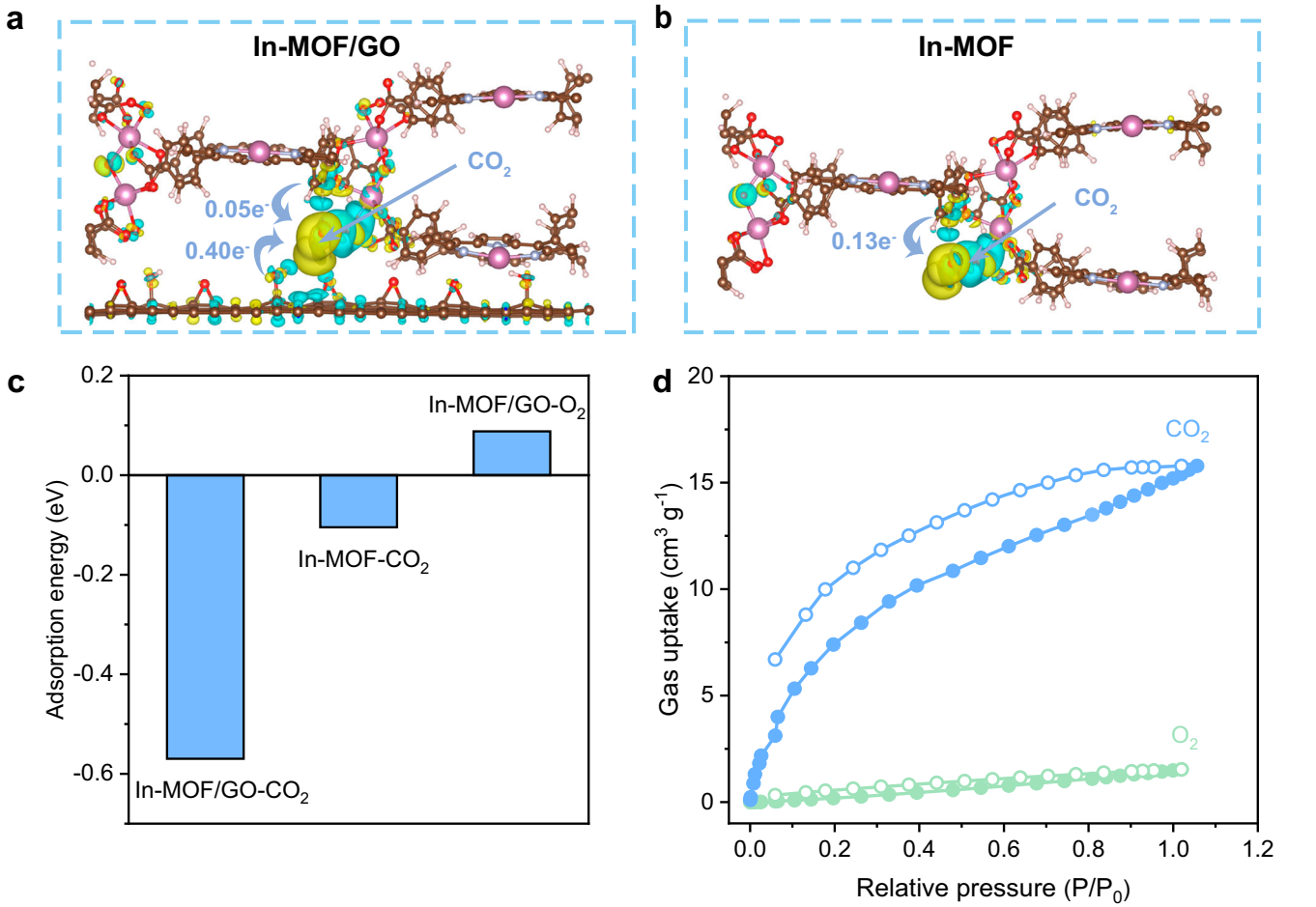

Fig. 4 | Investigation of CO_2 adsorption on In-MOF/GO. Calculated charge difference when CO_2 adsorbed on (**a**) In-MOF/GO and (**b**) self-supported In-MOF; yellow regions represent regions of electron accumulation, whereas blue regions denote areas of electron depletion. **c** Calculated adsorption energy for CO_2 and O_2 on In-MOF/GO and self-supported In-MOF. **d** Adsorption–desorption curves of CO_2 and O_2 on In-MOF/GO. Source data for Fig. 4c, d are provided as a Source Data file.

at 1658 cm^{-1} (Fig. 5a) can be attributed to the OCO vibration in the carboxylate-coordinated In-node (COO-In)[39]. The depletion of the carboxylate-related band at 1658 cm^{-1} is accompanied by the growth of the band at 1760 cm^{-1}. This is a characteristic of the OCO vibration in carboxylic acid and is attributed to the protonated form of carboxylate. Considering the theoretical prediction and XPS results that in the hybrid structure of In-MOF/GO, the electron transfer from GO to In-MOF moiety, it can be speculated that upon illumination, the In-node in In-MOF trapped the photogenerated electrons and being reduced. The reduced valance state of In results in reduced coordination numbers, causing the partial dissociation of the coordinated carboxylates (IR band at 1658 cm^{-1}), which were further by protons released from water oxidation to form carboxylic acid (IR band at 1760 cm^{-1}). The FT-IR results confirm that the In nodes in the In-MOF are the electron-enriched sites that are formed during photocatalytic reactions and are available for subsequent CO_2 reduction. Notably, the structural variations in the In-nodes are reversible. After cessation of illumination, the intensities at 1658 and 1760 cm^{-1} can be observed to recover, indicating restoration of the initial structure of the In-nodes (black spectrum in Fig. 5b).

The in situ FTIR-IR results also confirm that this tandem process was not affected by the presence or absence of O_2. When the photocatalytic CO_2 reduction is conducted under aerobic conditions (atmosphere: 20% O_2, 10% CO_2 and 70% Ar, saturated with D_2O), the intensity ratio between 1658 and 1760 cm^{-1} bands can be observed to vary (Fig. 5d). The corresponding intensity depletion of the D_2O-related band and appearance of CO_2RR intermediates-related bands can also be clearly observed (Fig. 5d). All emerged bands display an analogous behavior similar to those of the corresponding bands observed under anaerobic conditions (Fig. 5b). The observed similarities in the behavior of the bands confirm that the catalyst under study retains its efficiency in performing photocatalytic reactions, even under aerobic conditions. Based on in situ FT-IR spectroscopy, the mechanism of photocatalytic CO_2 reduction process on In-MOF/GO is depicted in Fig. 5e. It can be concluded that the In-node in the In-MOF/GO heterostructure plays an important role in both CO_2 capture and reduction. CO_2 is initially captured by the hydroxyl groups of the In-nodes. The captured CO_2 is then reduced to *COOH at the photo-reduced In-nodes, leading to the generation of CO, and the reduced In-nodes recovers for the next catalytic cycle.

Fabrication of a heterostructure between GO and In-MOF is also essential for accelerating CO_2 reduction. The theoretical calculations (Fig. 4a) demonstrate a more significant electron transfer to the CO_2 adsorbed on an In-MOF/GO heterostructure than on a self-supported In-MOF, activating chemically inert CO_2. Further simulation of CO_2 reduction to *COOH via coupled electron/proton transfer shows that the energy barrier for this step on an In-MOF/GO heterostructure is 3.06 eV, which is 0.56 eV lower than that on a self-supported In-MOF (Supplementary Data 1, Supplementary Figs. 23, 24, 25 and 26). This substantial difference in energy barriers indicates that CO_2 reduction proceeds more easily on the In-MOF/GO heterostructure, further highlighting the remarkable efficacy of in situ fabricated In-MOF/GO heterostructures in photocatalytic applications.

https://doi.org/10.1038/s41467-024-55753-2

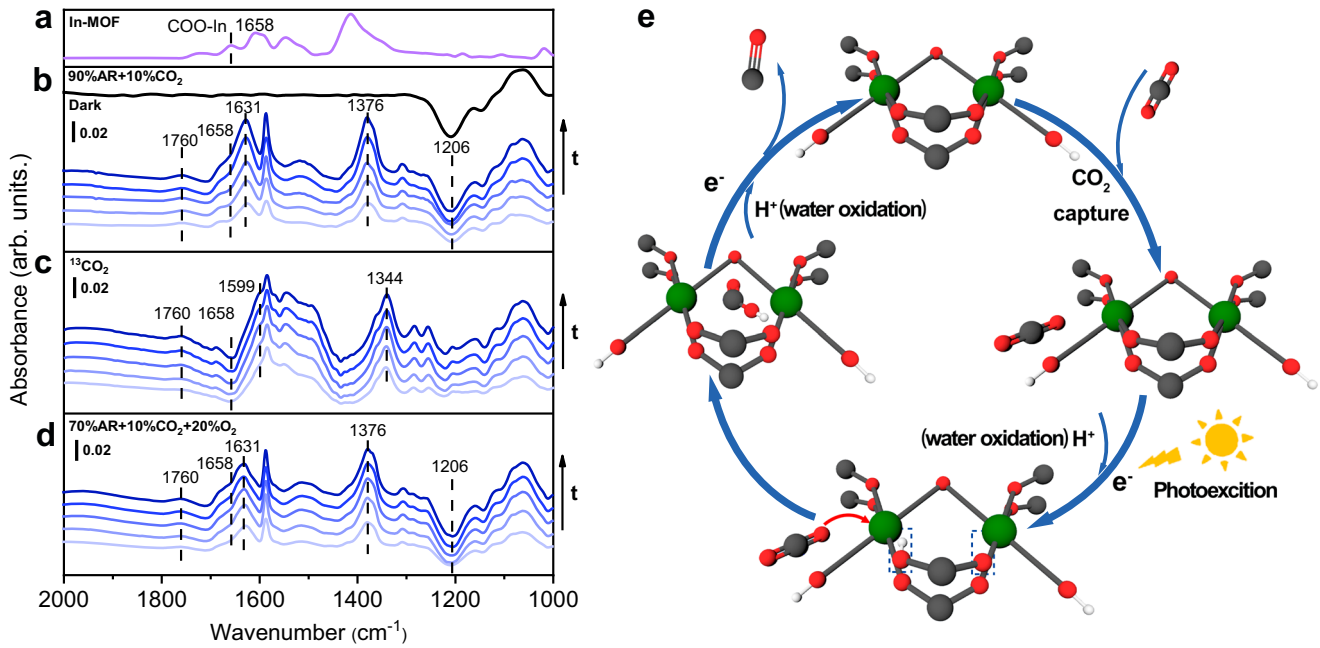

Fig. 5 | Monitoring photocatalytic CO_2 reduction on In-MOF/GO using in situ FT-IR spectroscopy. a Reference FT-IR spectra of self-supported In-MOF with KBr as background; In situ FT-IR spectra collected during the photocatalytic CO_2 reduction on In-MOF/GO under **b** 10% CO_2 and 90% Ar, **c** 100% $^{13}CO_2$, and **d** 10% CO_2, 20% O_2 and 70% Ar atmospheres. The FT-IR spectra shown in (**a**–**d**) were collected per 0.6 s (bottom to top); the total illumination time was 6 s. The top spectrum in (b) was collected after the illumination was terminated to show the reversible structural alternation of the catalyst. The background for (**b**–**d**) was collected right before illumination for each sample. **e** Schematic illustration of the photocatalytic CO_2 reduction on one structural unit of In-MOF; In, C, O, and H are shown as green, gray, red and white circles, respectively. Source data for Fig. 5a–d are provided as a Source Data file.

Discussion

In summary, we presented an in situ growth procedure to fabricate an In-MOF/GO heterostructure. The In-MOF/GO heterostructures can be used as photocatalysts to directly convert environmental CO_2. They enabled a tandem process involving CO_2 capture and selective photocatalytic reduction of low CO_2 concentrations even in the presence of air-level O_2. The experimental results demonstrated that the integrated system of In-MOF/GO catalysts with floatable and porous substrates forming artificial leaves can be utilized in open water environments. The design of the floatable artificial leaves enabled effective coupling between energy conversion (conversion of environmental CO_2) and water purification. This further facilitated effective COD reduction in natural water bodies along with CO_2 reduction, meeting the class I water standard of China. The floatable photocatalytic devices enable adaptable deployment based on exhaust emissions characteristics and light availability, rendering them suitable for various site conditions and capable of meeting diverse treatment demands.

Methods

Chemicals and materials

Indium (III) nitrate (In $(NO_3)_3$) and tetrakis (4-carboxylpheny) porphyrin (TCPP) were purchased from Shanghai Macklin Biochemical Co., Ltd. Single layer graphene oxide (GO, single layer ratio: approx. 90%) was purchased from J&K Scientific. Cetyltrimethylammonium bromide (CTAB) were purchased from Aladdin. N, N-Dimethylformamide (DMF), ethanol and acetone were purchased from Concord Technology (Tianjin) Co., Ltd. $^{13}CO_2$ ($^{13}C > 99\%$, $^{18}O < 2\%$) was purchased from Cambridge Isotope Laboratories. All the chemicals were analytical grade and used without further purification. Deionized water was prepared with a Milli-Q purification system and used throughout all the experiments.

Synthesis of In-MOF

The In-MOF nanosheet was prepared by a surfactant-assisted synthetic method[28,29]. Typically, TCPP (50 mg, 0.07 mmol), indium (III) nitrate (46.5 mg, 0.149 mmol) and CTAB (200 mg) were dispersed in deionized water (3.15 mL). The resulting suspension was sonicated for 10 min at room temperature, then transferred into a 25 mL of Teflon lined autoclave and heated at 120 °C for 16 h. After cooling down to room temperature, the product was collected by centrifugation at 10,000 rpm for 5 min, washed twice with DMF (2 × 20 mL) and twice with acetone (2 × 20 mL) in order to remove the unreacted precursors and the excess CTAB molecules. Finally, the solids were dried under vacuum at 80 °C.

In situ growth of In-MOF on GO

Before the synthesis of In-MOF/GO, solution A and B were prepared first for further use. Solution A: 1 mg of $In(NO_3)_3$ was dissolved in 2 mL DMF/EtOH (V/V = 3/1) solution. Solution B: 1 mg of TCPP was dissolved in 2 mL DMF/EtOH (V/V = 3/1) solution. Then in a typical synthesis, 5 mg of GO (single layer) was dispersed in a 25 mL three-neck bottle containing 10 mL DMF/EtOH (V/V = 3/1) solution by sonication. After that, the bottle was sealed and preheated in an oil bath at 90 °C for 10 min. Under stirring, 1 mL of solution A and solution B were separately injected at the rate of 0.25 mL/h by using a two-channel syringe pump. When the reaction was finished, the products were collected by centrifuge, and washed three times with ethanol. Finally, the product was dried at 60 °C in vacuum for 12 h.

Ex situ assembling of pre-crystalized In-MOF with GO

1 mg of as-synthesized In-MOF was dispersed in 2 mL DMF/EtOH (V/V = 3/1) solution. Then in a typical synthesis, 5 mg of GO (single layer) was dispersed in a 25 mL of three-neck bottle containing 10 mL DMF/EtOH (V/V = 3/1) solution by sonication. After that, the bottle was sealed and preheated at 90 °C for 10 min in an oil bath. Under stirring,1 mL of the In-MOF dispersion was injected at a rate of 0.25 mL/h using a single-channel syringe pump. When the reaction was finished, the products were collected by centrifuge, and washed three times with ethanol. Finally, the product was dried at 60 °C in vacuum for 12 h.

Characterization

Transmission electron microscopy (TEM) images were obtained on Hitachi HT-7700 microscope. High-resolution transmission electron microscopy (HR-TEM) images and energy dispersive analysis of X-rays (EDX) element maps were obtained on JEOL JEM-F200 microscope at an accelerating voltage of 200 kV. Atomic force microscopy (AFM) research was obtained on NTEGRA spectra (NT-MDT). X-ray diffraction (XRD) patterns were carried out on a PANalytical Empyrean Focus X-ray diffractometer with Cu Kα radiation (λ = 1.5405 Å). X-ray photoelectron spectroscopy (XPS) was conducted on a PHI Quantera SXM X-ray photoelectron spectrometer equipped with an Al X-ray excitation source (1486.6 eV). The binding energies (BE) were corrected by the C1*s* peak at 284.8 eV. Fourier Transform infrared spectroscopy (FT-IR) was performed on a Bruker Vertex 70 V spectrometer equipped with a narrow band HgCdTe detector. Gas (CO_2 or O_2) adsorption-desorption isotherms were analyzed by TriStar II plus 3.03 flex adsorption apparatus (Micromeritics, USA). Samples were degassed at 100 °C for 12 h under vacuum before analysis. The temperature-programmed desorption (TPD) tests were performed using a Micromeritics AutoChem II 2920 instrument. The Electron paramagnetic resonance (EPR) spectra were collected on an E500 spectrometer (Bruker, Switzerland).

Activity test of the photocatalytic CO_2 reduction

In a typical activity test, 2 mg of In-MOF/GO photocatalysts were dispersed in 5 mL deionized H_2O by sonication, and then the suspension was vacuum filtrated to load the photocatalyst onto a polytetrafluoroethylene (PTFE) membrane of 3 cm diameter and a thickness of 180 μm. The PTFE membrane has a light transmittance of 20%. The PTFE membrane loaded with photocatalyst is placed within a quartz cell containing 50 mL of deionized water or lake water collected from Beijing Olympic Park, the membrane was floated on the water surface and the side loading photocatalysts faced down. Subsequently, this assembly is positioned inside a sealed reactor equipped with quartz windows to enable the illumination of the floating catalyst membrane (Supplementary Fig. 14). Before irradiation, the reactor was purged with a simulated combustion flue gas composed of 10% CO_2, 20% O_2 and 70% Ar at a constant flow rate of 50 mL/min for a total period of 30 minutes. A 300 W Xe lamp (Beijing Perfectlight PLS-SXE300C) with a 420 nm cut-off filter was used as the visible light source maintaining a constant light intensity of 300 mW·cm^{-2}. During the reaction, the gas products were analyzed by a gas chromatograph (GC7920-TF2Z) equipped with thermal conductivity and flame ionization detectors. $^{13}CO_2$ isotope labeling experiment was conducted under the same condition, and the isotope-labeled gas products were quantified by GC-MS (Gas chromatography-mass spectrometry, Agilent Technologies 7890A-5957C) with triple-axis detector.

H_2O_2 detection

The hydrogen peroxide (H_2O_2) was quantified by DPD-POD method[30]. The DPD (N, N-diethyl-p-phenylenediamine) solution was prepared by dissolving 0.1 g of DPD in 10 mL of 0.05 M H_2SO_4. The POD (peroxidase from horseradish) solution was prepared by dissolving 10 mg of POD in 10 mL of deionized water. A phosphate buffer solution was prepared by adding 6 g of potassium dihydrogen phosphate and 1.68 g of dipotassium phosphate to 100 mL of deionized water. All prepared solutions were stored in a refrigerator. For the measurement of H_2O_2, 2 mL of the photocatalyzed solution was mixed with 0.4 mL of the phosphate buffer, 3 mL of water, 0.05 mL of DPD, and 0.05 mL of POD, followed by shaking for 45 seconds. The resulting solution was analyzed using UV-vis spectroscopy. When the generated H_2O_2 exceeded the detection limit, a pink-colored solution was obtained, and the H_2O_2 concentration was determined by measuring the absorbance at approximately 552 nm.

Calculation details

All calculations in this work were performed using CP2K[40] with the PBE exchange-correlation functional[41] at the Generalized Gradient Approximation (GGA) level. The model consists of an orthogonal cubic cell with lattice dimensions of 16.7, 33.5, and 28.1 angstroms in the a, b, and c directions, respectively. The vacuum layer in the c direction is over 15 angstroms, ensuring no interaction between images. Due to the large size of the lattice, calculations were performed using the gamma point. A cutoff energy of 400 eV was used. Geometric optimization and frequency calculations were corrected for dispersion interactions using Grimme's DFT-D3 method[42]. The convergence criteria for root mean square displacement and root mean square forces were 0.003 Bohr and 0.0006 Hartree/Bohr, respectively. The energy convergence criterion was 10^{-5} eV. Frequencies were obtained by diagonalizing the numerical Hessian, which was calculated using a finite difference approximation with a step size of 0.01 Bohr. Frequency calculations were performed on the adsorbed molecules only, with the catalyst substrate fixed. Gibbs free energy corrections were calculated using the Shermo[43]. For processes involving h^+ and e^-, the Gibbs free energy changes were calculated using the Computational Hydrogen Electrode (CHE) model developed by Nørskov et al.[44,45]. Gibbs free energy analyses were conducted under standard conditions (pH = 0, 298.15 K, 1 atm) with U = 0 V.

Data availability

The raw data for each curve in Figs. 2c, 3b–g, 4c–d, 5a–d and Supplementary Figs. generated in this study are provided in the Source Data file. Source data are provided with this paper.

References

1. Dogutan, D. et al. Artificial photosynthesis at efficiencies greatly exceeding that of natural photosynthesis. *Acc. Chem. Res.* **52**, 3143–3148 (2019).
2. Kim, D. et al. Artificial photosynthesis for sustainable fuel and chemical production. *Angew. Chem. Int. Ed.* **54**, 3259–3266 (2015).
3. Jiang, Z. et al. Filling metal-organic framework mesopores with TiO_2 for CO_2 photoreduction. *Nature* **586**, 549–554 (2020).
4. Zhang, L. et al. Decoupled artificial photosynthesis. *Angew. Chem. Int. Ed.* **62**, e202219076 (2023).
5. Lv, J. et al. Solar utilization beyond photosynthesis. *Nat. Rev. Chem.* **7**, 91–105 (2023).
6. Kim, J. H. et al. Toward practical solar hydrogen production–an artificial photosynthetic leaf-to-farm challenge. *Chem. Soc. Rev.* **48**, 1908–1971 (2019).
7. Andrei, V. et al. Floating perovskite-$BiVO_4$ devices for scalable solar fuel production. *Nature* **608**, 518–522 (2022).
8. Zhao, Y. et al. Two-dimensional-related catalytic materials for solar-driven conversion of COx into valuable chemical feedstocks. *Chem. Soc. Rev.* **48**, 1972–2010 (2019).
9. Huang, D. S. et al. Electrosynthesis of urea by using Fe_2O_3 nanoparticles encapsulated in a conductive metal-organic framework. *Nat. Synth.* **3**, 1404–1413 (2024).
10. Chen, H. Y. et al. Integration of plasmonic Ag (I) clusters and Fe (II) porphyrinates into metal-organic frameworks for efficient photocatalytic CO_2 reduction coupling with photosynthesis of pure H_2O_2. *Angew. Chem. Int. Ed.* **63**, e202412553 (2024).
11. Saito, D. et al. Photocatalysis of a dinuclear Ru(II)-Re(I) complex for CO_2 reduction on a solid surface. *J. Am. Chem. Soc.* **142**, 19249–19258 (2020).
12. Yu, X. et al. Eosin Y-functionalized conjugated organic polymers for visible light-driven CO_2 reduction with H_2O to CO with high efficiency. *Angew. Chem. Int. Ed.* **58**, 632–636 (2019).
13. Dilla, M. et al. The fate of O_2 in photocatalytic CO_2 reduction on TiO_2 under conditions of highest purity. *Phys. Chem. Chem. Phys.* **21**, 15949–15957 (2019).

14. Chen, Y. et al. A highly active, CO_2-tolerant electrode for the oxygen reduction reaction. *Energy Environ. Sci.* **11**, 2458–2466 (2018).
15. Ma, Y. et al. Selective photocatalytic CO_2 reduction in aerobic environment by microporous Pd-porphyrin-based polymers coated hollow TiO_2. *Nat. Commun.* **13**, 1400 (2022).
16. Xie, S. et al. Facilitated photocatalytic CO_2 reduction in aerobic environment on a copper-porphyrin metal-organic framework. *Angew. Chem. Int. Ed.* **62**, e202216717 (2023).
17. Nakajima, T. et al. Photocatalytic reduction of low concentration of CO_2. *J. Am. Chem. Soc.* **138**, 13818–13821 (2016).
18. Kreft, S. et al. Improving selectivity and activity of CO_2 reduction photocatalysts with oxygen. *Chem* **5**, 1818–1833 (2019).
19. Lu, Z. et al. High-efficiency oxygen reduction to hydrogen peroxide catalysed by oxidized carbon materials. *Nat. Catal.* **1**, 156–162 (2018).
20. Zhang, W. et al. Z-Scheme photocatalytic systems for carbon dioxide reduction: where are we now? *Angew. Chem. Int. Ed.* **59**, 22894–22915 (2020).
21. Lu, K. et al. Rationally designed transition metal hydroxide nanosheet arrays on graphene for artificial CO_2 reduction. *Nat. Commun.* **11**, 5181 (2020).
22. Xu, F. et al. Unique S-scheme heterojunctions in self-assembled TiO_2/$CsPbBr_3$ hybrids for CO_2 photoreduction. *Nat. Commun.* **11**, 4613 (2020).
23. Kajiwara, T. et al. Photochemical reduction of low concentrations of CO_2 in a porous coordination polymer with a ruthenium (II)-CO complex. *Angew. Chem. Int. Ed.* **55**, 2697–2700 (2016).
24. Wagner, A. et al. Towards molecular understanding of local chemical environment effects in electro- and photocatalytic CO_2 reduction. *Nat. Catal.* **3**, 775–786 (2020).
25. Markewitz, P. et al. Worldwide innovations in the development of carbon capture technologies and the utilization of CO_2. *Energy Environ. Sci.* **5**, 7281–7305 (2012).
26. Schwender, J. et al. Rubisco without the Calvin cycle improves the carbon efficiency of developing green seeds. *Nature* **432**, 779–782 (2004).
27. Krishnamoorthy, K. et al. The chemical and structural analysis of graphene oxide with different degrees of oxidation. *Carbon* **53**, 38–49 (2013).
28. Leng, F. et al. Boosting photocatalytic hydrogen production of porphyrinic MOFs: the metal location in metalloporphyrin matters. *ACS Catal* **8**, 4583–4590 (2018).
29. Zhang, Z. et al. Ultra-stable two-dimensional metal-organic frameworks for photocatalytic H_2 production. *Nanoscale* **14**, 7146–7150 (2022).
30. Xie, Y. et al. A floatable photocatalyst to synergistically promote CO_2 reduction and water oxidation by creating oriented charge separation across a tri-phase interface. *Energy Environ. Sci* **17**, 4725–4734 (2024).
31. Wang, Y. et al. Two-dimensional-on-three-dimensional metal-organic frameworks for photocatalytic H_2 production. *Angew. Chem. Int. Ed* **134**, e202211031 (2022).
32. Kuttassery, F. et al. A molecular Z-scheme artificial photosynthetic system under the bias-free condition for CO_2 reduction coupled with two-electron water oxidation: photocatalytic production of CO/HCOOH and H_2O_2. *Angew. Chem. Int. Ed.* **135**, e202308956 (2023).
33. Samanta, S. et al. Surface modified C, O co-doped polymeric g-C_3N_4 as an efficient photocatalyst for visible light assisted CO_2 reduction and H_2O_2 production. *Appl. Catal. B- Environ.* **259**, 118054 (2019).
34. Wang, Y. et al. Hydroxide ligands cooperate with catalytic centers in metal-organic frameworks for efficient photocatalytic CO_2 reduction. *J. Am. Chem. Soc.* **140**, 38–41 (2018).
35. Wang, W. et al. Accelerated photocatalytic carbon dioxide reduction and water oxidation under spatial synergy. *Angew. Chem. Int. Ed.* **63**, e202317969 (2024).
36. Zhu, J. et al. Asymmetric triple-atom sites confined in ternary oxide enabling selective CO_2 photothermal reduction to acetate. *J. Am. Chem. Soc.* **143**, 18233–18241 (2021).
37. Di, J. et al. Surface local polarization induced by bismuth-oxygen vacancy pairs tuning non-covalent interaction for CO_2 photoreduction. *Adv. Energy Mater.* **11**, 2102389 (2021).
38. Wang, S. et al. Intermolecular cascaded π-conjugation channels for electron delivery powering CO_2 photoreduction. *Nat. Commun.* **11**, 1149 (2020).
39. Nam, D. H. et al. Metal-organic frameworks mediate Cu coordination for selective CO_2 electroreduction. *J. Am. Chem. Soc.* **140**, 11378–11386 (2018).
40. Kühne, T. et al. CP2K: An electronic structure and molecular dynamics software package-Quickstep: Efficient and accurate electronic structure calculations. *J. Chem. Phys.* **152**, 194103 (2020).
41. Perdew, J. et al. Generalized gradient approximation made simple. *Phys. Rev. Lett.* **77**, 3865–3868 (1996).
42. Grimme, S. et al. A consistent and accurate ab initio parametrization of density functional dispersion correction (DFT-D) for the 94 elements H-Pu. *J. Chem. Phys.* **132**, 154104 (2010).
43. Lu, T. et al. A general code for calculating molecular thermodynamic properties. *Comput. Theor. Chem.* **1200**, 113249 (2021).
44. Nørskov, J. et al. Origin of the overpotential for oxygen reduction at a fuel-cell cathode. *J. Phys. Chem. B* **108**, 17886–17892 (2004).
45. Nørskov, J. et al. Trends in the exchange current for hydrogen evolution. *J. Electrochem. Soc.* **152**, J23 (2005).

Acknowledgements

This work was supported by the National Natural Science Foundation of China (Nos. 22222609 and 22321004), National Key Research and Development Program of China (No. 2020YFA0710303) and CAS Project for Young Scientists in Basic Research (No. YSBR-004).

Author contributions

H.S. created the concept and designed the overall project. Z.Z. designed and conducted the experiments, analyzed the data and drafted the article. Y.W. discussed the materials synthesis and characterization. Y.X., Q.Z., Q.H., X. H. and B. Z. discussed performance testing. J.Z., W.S., C.C. and Tsukamoto assisted with the paper revision. All the authors discussed and revised the paper.

Competing interests

The authors declare no competing interests.

Additional information

Supplementary information The online version contains supplementary material available at https://doi.org/10.1038/s41467-024-55753-2.

Correspondence and requests for materials should be addressed to Hua Sheng.

Peer review information *Nature Communications* thanks Pei-Qin Liao, Wei Huang, and the other, anonymous, reviewer(s) for their contribution to the peer review of this work. A peer review file is available.